

## Article

# Combination of Metal Oxide and Polytriarylamine: A Design Principle to Improve the Stability of Perovskite Solar Cells

Marina M. Tepliakova <sup>1,\*</sup>, Alexandra N. Mikheeva <sup>1</sup>, Pavel A. Somov <sup>1</sup>, Eugene S. Statnik <sup>1</sup>, Alexander M. Korsunsky <sup>2,1</sup> and Keith J. Stevenson <sup>1</sup>

<sup>1</sup> Center for Energy Science and Technology (CEST), Skolkovo Institute of Science and Technology, Nobel st. 3, 143026 Moscow, Russia; sashulya-miheeva@mail.ru (A.N.M.); Pavel.Somov@skoltech.ru (P.A.S.); Eugene.Statnik@skoltech.ru (E.S.S.); K.Stevenson@skoltech.ru (K.J.S.)

<sup>2</sup> Multi-Beam Laboratory for Engineering Microscopy, Department of Engineering Science, University of Oxford, Parks Road, Oxford OX1 3PJ, UK; A.Korsunsky@skoltech.ru

\* Correspondence: marina.tepliakova@skoltech.ru

**Abstract:** In the last decade, perovskite photovoltaics gained popularity as a potential rival for crystalline silicon solar cells, which provide comparable efficiency for lower fabrication costs. However, insufficient stability is still a bottleneck for technology commercialization. One of the key aspects for improving the stability of perovskite solar cells (PSCs) is encapsulating the photoactive material with the hole-transport layer (HTL) with low gas permeability. Recently, it was shown that the double HTL comprising organic and inorganic parts can perform the protective function. Herein, a systematic investigation and comparison of four double HTLs incorporating polytriarylamine and thermally evaporated transition metal oxides in the highest oxidation state are presented. In particular, it was shown that MoO<sub>x</sub>, WO<sub>x</sub>, and VO<sub>x</sub>-based double HTLs provided stable performance of PSCs for 1250 h, while devices with NbO<sub>x</sub> lost 30% of their initial efficiency after 1000 h. Additionally, the encapsulating properties of all four double HTLs were studied in trilayer stacks with HTL covering perovskite, and insignificant changes in the absorber composition were registered after 1000 h under illumination. Finally, it was demonstrated using ToF-SIMS that the double HTL prevented the migration of perovskite volatile components within the structure. Our findings pave the way towards improved PSC design that ensures their long-term operational stability.

**Keywords:** perovskite solar cells; hole-transport layer; stable photovoltaics; secondary ion spectroscopy



**Citation:** Tepliakova, M.M.; Mikheeva, A.N.; Somov, P.A.; Statnik, E.S.; Korsunsky, A.M.; Stevenson, K.J. Combination of Metal Oxide and Polytriarylamine: A Design Principle to Improve the Stability of Perovskite Solar Cells. *Energies* **2021**, *14*, 5115. <https://doi.org/10.3390/en14165115>

Academic Editor: Bashir A. Arima

Received: 2 August 2021

Accepted: 16 August 2021

Published: 19 August 2021

**Publisher's Note:** MDPI stays neutral with regard to jurisdictional claims in published maps and institutional affiliations.



**Copyright:** © 2021 by the authors. Licensee MDPI, Basel, Switzerland. This article is an open access article distributed under the terms and conditions of the Creative Commons Attribution (CC BY) license (<https://creativecommons.org/licenses/by/4.0/>).

## 1. Introduction

The first application of a lead halide perovskite material in photovoltaic devices was reported in 2009, when perovskite was used as a light harvester for dye-sensitized solar cells, showing 3.8% efficiency [1]. Since then, tremendous improvement in the power conversion efficiency up to the current 25.5% record has occurred [2]. The liquid electrolyte employed in the first reported work was soon substituted with the solid hole-transport layer (HTL) material Spiro-OMeTAD, giving the all-solid-state perovskite solar cells (PSCs) 9.7% efficiency and 500 h stability [3]. Furthermore, the classical approach of using a mesoporous TiO<sub>2</sub> scaffold as an electron transport layer (ETL) was found to be redundant, as the perovskite material itself demonstrated impressive charge transport characteristics [4]. Thus, mesoporous ETLs were replaced by compact ETLs, resulting in a cheaper and easier-to-assemble planar structure.

After achieving reasonable efficiencies of more than 15%, the work on improving the long-term stability of perovskite solar cells began. The degradation mechanism of perovskite solar cells remains the subject of intense investigation. Nevertheless, several aspects of the complex mechanisms have been revealed in the literature.

One of the aspects of PSC degradation is the reversible decomposition of perovskite material occurring under operational conditions with the formation of volatile decomposition products (e.g.,  $\text{CH}_3\text{NH}_2$ ,  $\text{I}_2$ ,  $\text{NH}_3$ ) [5,6]. The migration of these volatile species from the perovskite structure leads to irreversible degradation of the photoactive layer and respective deterioration of the device performance. Therefore, covering the absorber layer with materials with low gas permeability layer is the key to PSC stability improvement. In the standard configuration of PSC, the material applied on top of the perovskite layer is represented by the HTL.

The exceptional potential in providing selective hole extraction and efficient encapsulation of perovskite material was recently elucidated for the combination of organic and inorganic p-type materials [7]. In such organic–inorganic double HTLs, the organic counterpart is usually represented by various p-type polymers and low-molecular-weight HTL materials [8–10]. The well-adjusted energy levels of such materials matching that of perovskite enable selective hole extraction. As for inorganic components, the transition metals in the highest oxidation states were found to have significant potential. Taking into consideration the fact that metals in the highest oxidation state may partially lose oxygen during the deposition process or undergo reduction of the transition metal during “mixing” with the adjacent layers, they will be referred to as  $\text{MO}_x$ , where M stands for the transition metal. Despite the fact that the work function of partially reduced material may be insignificantly shifted, the properties of such layers are highly reproducible, and the transport characteristics may even improve due to the doping effect(s) [11,12].

In the recent literature, it was shown that  $\text{MO}_x$  can dope organic materials, thus improving their hole mobility and tuning work functions [13]. The study of thin films with configuration crystal  $\text{Si}/\text{MO}_x$  ( $M = \text{W}, \text{V}, \text{Mo}$ ) using time-of-flight secondary ion mass spectrometry (ToF-SIMS) revealed the passivating effect of these oxides. In brief, it was demonstrated that the  $\text{SiO}_x$  thin layer and reduced  $\text{MO}_x$  layers appeared between Si and  $\text{MO}_x$ , leading to Fermi level equilibration across the interface [14]. In addition, such advantages of  $\text{MO}_x$ , with high conductivity and the ability to form a smooth pinhole-free layer with organic HTLs, enable high efficiencies in PSCs of more than 20% [15,16]. Additionally, the high transparency of  $\text{MO}_x$  permits their application in inverted PSC configurations [17]. However, most importantly, the incorporation of the  $\text{MO}_x$  layer was found to be efficient in improving the operational stability of PSCs [18].

In sum, the organic–inorganic HTL approach allows the fabrication of efficient and long-term stable PSCs. In this regard, there is great interest in identifying inorganic metal oxides that are most capable of improving PSCs’ overall performance.

In the present study, the comparison of four metal oxides as inorganic counterparts of double HTL was conducted. In particular, the efficiency and stability were evaluated for PSCs incorporating double HTLs bearing an oxide of one of the four transition metals (Mo, V, W, and Nb), in combination with state-of-the-art polymer polytriarylamine (PTAA) [19]. As mentioned above, such combinations are expected to provide good encapsulation properties preventing the release of volatiles from the photoactive material and additionally protect the photoactive layer from the possible interaction with moisture and oxygen ingress under ambient conditions (Figure 1a).

There are numerous reports on the application of  $\text{MoO}_x$  [20–26] and  $\text{VO}_x$  [16,22,27–31] as HTLs in perovskite solar cells.  $\text{WO}_x$  was previously reported as a component of an efficient double-layer ETL [32] and HTLs [8,33,34]. This ability of  $\text{WO}_x$  to function as both electron- and hole-transport layers was also demonstrated for the case of a light-emitting diode, where partial oxidation of  $\text{WO}_3$  led to the appearance of new sub-gap energy levels, which facilitated electron-transfer mechanisms [35].  $\text{NbO}_x$  was previously reported only as the ETL material; however, we added this oxide to the studied set in order to investigate the influence of  $\text{MO}_x$  energy levels on the performance of perovskite solar cells. The energy level diagram for materials studied in this work is summarized in Figure 1b [13]. According to literature, the energy levels of studied metal oxides are not in alignment for efficient hole

transport. Therefore, the tunneling charge-transfer mechanism is hypothesized in metal oxides.

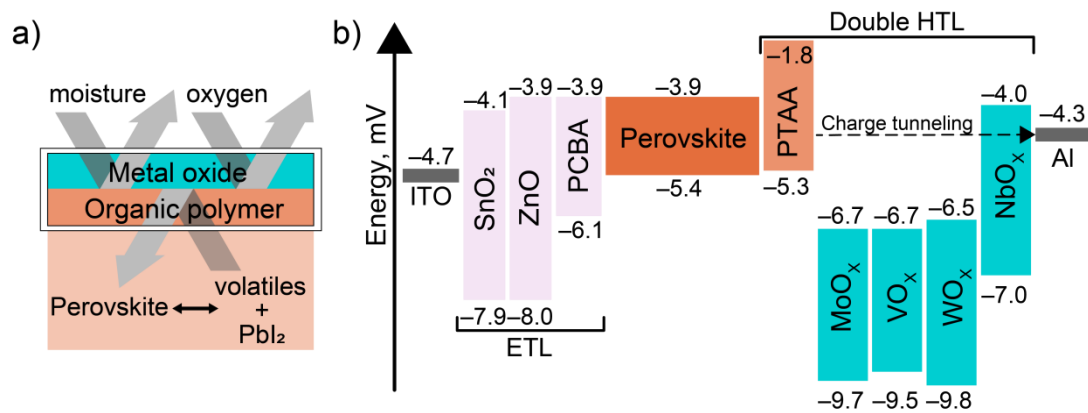


**Figure 1.** (a) Schematic illustration of the double organic-inorganic HTL encapsulating properties; (b) energy-level diagram of the materials used in this work.

Despite the rising popularity of cheap solution-based deposition methods applied for metal oxides, it was decided to concentrate on thermal evaporation under reduced pressure or physical vapor deposition (PVD). This method firstly was chosen because it is more compatible with upscaling compared to solution processing using the spin-coating typically applied for fabrication of research cells in laboratories. In addition, it recently was shown for organic HTLs that thermal evaporation is a more reliable method than spin-coating, because the possible trapping of solvent in the solution-processed film, with its further uncontrollable evaporation, may lead to the formation of defects in the layer [36]. Finally, the deposition using solution processing of metal oxides implies the application of alcohols, which cannot be performed in the inert atmosphere of gloveboxes, while any operations performed on the unencapsulated perovskite layer under ambient conditions may lead to a negative impact on the absorber layer from the moisture and oxygen with formation of undesirable products such as PbO, HI, and others [37,38]. In this work, we present the comparison of four metal oxides deposited using PVD as inorganic counterparts of double HTL, which enabled efficient encapsulation of the perovskite material, thus providing stable performance of perovskite solar cells.

## 2. Materials and Methods

All solvents and reagents were purchased from Sigma-Aldrich (Darmstadt, Germany) or Acros Organics (Geel, Belgium), if not otherwise stated, and used as received or purified according to standard procedures.

### 2.1. Device and Glass Fabrication

After etching the part of the ITO from Kintec (Kowloon, Hong Kong) with HCl and Zn to create a pattern for the solar cell, samples were cleaned using subsequent ultrasonication in isopropanol, water, and acetone, and then exposed to an air plasma treatment (50 W) for 5 min.

#### 2.1.1. ETL Deposition

The SnO<sub>2</sub> layer was spin-coated from 10% aqueous solution of nanoparticles from Alfa-Aesar (Haverhill, Massachusetts, USA), at 4000 rpm. The sample was further annealed at 150 °C for 20 min and moved to the glovebox. The samples were annealed in the glovebox at 100 °C for 10 min and cooled to the ambient temperature. The layer of 6,6-phenyl-C61 butyric acid (PCBA) synthesized according to the literature [39] was spin-coated from PCBA solution (0.2 mg/mL) in chlorobenzene at 3000 rpm. The structure of PCBA is given in Figure S1.

The ZnO solution was prepared by dissolving Zn acetate (100 mg) in monoethanolamine (33  $\mu$ L) and 2-methoxyethanol (1 mL) and spin-coated atop ITO at 3000 rpm. The samples were slowly heated from room temperature to 200 °C, annealed at 200 °C for 1 h, and cooled to room temperature. The  $\text{CH}_3\text{NH}_3\text{I}$  (MAI) solution (8 mg/mL in isopropanol) was spin-coated atop ZnO at 3000 rpm. The samples were heated up to 300 °C and annealed for 4 min. Afterward, the samples were transferred into the glovebox and heated at 100 °C for 5 min, and the PCBA was deposited as mentioned above.

### 2.1.2. Perovskite Deposition

The samples were annealed for 10 min at 100 °C and cooled down to the ambient temperature. The  $\text{CH}_3\text{NH}_3\text{PbI}_3$  ( $\text{MAPbI}_3$ ) perovskite ink with 1.4 M concentration was prepared by dissolving the stoichiometric quantities of MAI and  $\text{PbI}_2$  in DMF and NMP at 80% and 20%, respectively. For the experiment with trilayers, the perovskite concentration was reduced to 0.5 M to satisfy the limits of the absorption measurement equipment. The ink was spin-coated onto the cooled substrates at 4000 rpm, quenched with toluene after 20 s, and spanned for 40 s. The samples were left on the cool surface for 20 min, then heated slowly up to 80 °C and annealed for 5 min.

The  $\text{CsFAPbI}_3$  ink with 1.4 M concentration was prepared by dissolving CsI (99 mg),  $(\text{NH}_2)_2\text{CHI}$  (434 mg), and  $\text{PbI}_2$  (1474 mg) in DMF and DMSO at 85% and 15%, respectively. The ink was spin-coated at 4000 rpm and quenched with ethyl acetate at 17 s, and immediately placed onto the heater at 100 °C for 10 min of annealing.

### 2.1.3. Double-HTL Deposition and Top Electrodes

The hot PTAA (synthesized as described in the literature [40]) solution (6 mg/mL) was spin-coated on top of the perovskite ink at 3000 rpm (structure in Figure S1).

The metal oxide was thermally evaporated on the whole surface of the sample under reduced pressure. A tungsten boat was used as a holder for metal oxides. A pressure of  $10^{-5}$  mbar was reached using a turbo vacuum pump. The power of the source was increased slightly until an evaporation speed of 0.2 Å per second was stabilized. Further, the first 5 nm of the material was evaporated on the shutter, then the shutter was opened, and the evaporation proceeded with the rate maintained at the interval of 0.2–0.4 Å per second until the desired thickness was reached. For  $\text{MoO}_x$ ,  $\text{VO}_x$ ,  $\text{WO}_x$ , and  $\text{NbO}_x$ , the power of the source providing stable evaporation rates were 21, 23, 30, and 35%, respectively.

The part of the device intended for contact with the bottom electrode was mechanically cleaned from the top layers. The top electrodes (silver or aluminum) were thermally evaporated under reduced pressure through a shadow mask defining the device area as 0.08  $\text{cm}^2$ .

## 2.2. Device and Glass Characterization

The perovskite solar cells' characteristics were collected under simulated AM1.5G illumination (100  $\text{mW}/\text{cm}^2$ ), provided with a Newport Verasol AAA solar simulator and using Advantest 6240 A source-measurement units.

UV-vis spectra were measured in an inert atmosphere using an AvaSpec-2048-2UV-VIS fiber spectrometer integrated with an MBraun glovebox.

X-ray diffraction patterns were collected using a Bruker D8 instrument with a  $\text{Cu K}\alpha$  source.

The ToF-SIMS measurements were performed using a Tescan Solaris FIB-SEM microscope (AICF, Skoltech) under a pressure of  $5 \times 10^{-4}$  Pa using a focused gallium ion beam registering the secondary ions with a C-TOF detector (TOFWERK).

## 3. Results and Discussion

At the first step, the thickness optimization of four metal oxide layers was performed. For this purpose, PSCs with a classical configuration were fabricated (Figure 2a). In brief, the conductive indium tin oxide (ITO) electron-collecting electrode was covered with

solution-processed nanoparticles of SnO<sub>2</sub> as the ETL. Afterward, the thin layer of PCBA was spin-coated atop the ETL as a defect-passivating layer [39,41]. The CH<sub>3</sub>NH<sub>3</sub>PbI<sub>3</sub> perovskite layer was deposited from the solution, and the organic component of the double-layer polymer polytriarylamine (PTAA) synthesized using Suzuki polycondensation was spin-coated atop the perovskite layer [40]. Finally, one of the four metal oxides with various thicknesses was deposited on the whole surface using PVD, followed by the silver electrodes' evaporation through the shadow mask. The thicknesses, defined with a crystal quartz detector built into the evaporator were additionally verified using a height profile of the scratches made on metal oxide/glass samples collected with atomic force microscopy (AFM). A total of 16 devices with each thickness were fabricated to generate robust and reliable statistics. The distributions of power-conversion efficiencies (PCEs, %) along with the current-voltage characteristics, such as open-circuit voltages ( $V_{oc}$ , mV), short-circuit currents ( $J_{sc}$ , mA/cm<sup>2</sup>), and fill factors (FF, %) for the best devices are summarized in Figure 2b,c and Table 1.

**Table 1.** Distribution of PSC characteristics incorporating MO<sub>x</sub> with various thicknesses given as top (average ± standard deviation).

MO <sub>x</sub>	Thickness, nm	$V_{oc}$ , mV	$J_{sc}$ , mA/cm <sup>2</sup>	FF, %	PCE, %
MoO <sub>x</sub>	5	1037 (1020 ± 10)	22.3 (22.1 ± 0.2)	76 (72 ± 4)	17.3 (16.0 ± 1.0)
	10	1059 (1044 ± 9)	22.2 (21.3 ± 0.8)	77 (72 ± 2)	18.0 (16.0 ± 1.0)
	15	1045 (1034 ± 7)	21.6 (20.9 ± 0.4)	78 (74 ± 4)	17.2 (16.0 ± 1.0)
	20	1053 (1040 ± 50)	22.0 (22.0 ± 1.0)	84 (76 ± 5)	17.5 (16.0 ± 1.0)
VO <sub>x</sub>	5	1014 (1007 ± 9)	19.5 (19.4 ± 0.2)	71 (67 ± 5)	14.1 (13.0 ± 1.0)
	20	1028 (1020 ± 10)	22.2 (20.3 ± 0.7)	77 (74 ± 6)	16.1 (16.0 ± 1.0)
	30	1045 (1010 ± 20)	20.7 (19.2 ± 0.8)	78 (73 ± 4)	15.1 (14.4 ± 0.7)
WO <sub>x</sub>	45	1019 (1009 ± 9)	21.4 (20.1 ± 0.8)	78 (67 ± 4)	16.0 (14.0 ± 1.0)
	20	1037 (1020 ± 10)	22.0 (21.1 ± 0.4)	70 (68 ± 4)	15.7 (15.0 ± 1.0)
	30	991 (970 ± 30)	21.3 (21.2 ± 0.1)	68 (64 ± 3)	14.0 (13.4 ± 0.9)
	40	1010 (930 ± 40)	21.5 (20.9 ± 0.8)	70 (68 ± 4)	15.1 (14.0 ± 2.0)
NbO <sub>x</sub>	60	1037 (1000 ± 20)	21.5 (20.7 ± 0.5)	71 (63 ± 3)	15.2 (13.0 ± 1.0)
	10	359 (260 ± 60)	11.3 (10 ± 1.0)	29 (26 ± 1)	0.9 (0.6 ± 0.1)
	20	329 (300 ± 20)	11.1 (10.1 ± 0.6)	28 (26 ± 1)	0.9 (0.8 ± 0.1)
	30	1013 (1000 ± 300)	21.4 (19.0 ± 2.0)	61 (60 ± 10)	11.9 (10.0 ± 4.0)
	40	934 (500 ± 300)	20.4 (16.0 ± 2.0)	59 (40 ± 10)	11.2 (3.0 ± 3.0)

First, the optimal thickness of devices with MoO<sub>x</sub> was identified. For this purpose, 10 and 20 nm thicknesses were selected for the first experiment. The maximum efficiency (18.0%) of PSCs with 10 nm MoO<sub>x</sub> layers was slightly superior to that of devices with 20 nm thick MoO<sub>x</sub> layers (17.5%). In order to expand the search range for the optimal thickness, additional devices using 5 and 15 nm thick MoO<sub>x</sub> were prepared. According to the results, the 5 nm difference in the thickness of MoO<sub>x</sub> did not lead to significant deviations in the device performance, which could be also concluded from the similar average efficiency of 16% for each type of device. Therefore, for MoO<sub>x</sub>, the value of 10 nm, which enabled the highest efficiency in the perovskite solar cells, was chosen as optimal.

In the next step, the optimization of VO<sub>x</sub> thickness was performed. Preliminary perovskite solar cells incorporating the material were studied for stability using 15, 30, and 45 nm thicknesses of VO<sub>x</sub> (Figure S2). It was observed that the 15 nm thickness enabled the worst stability in devices, which was probably due to poor coverage of the perovskite

surface, resulting in the formation of paths for volatile perovskite component migration. The devices incorporating  $\text{VO}_x$  with two other selected thicknesses demonstrated a similar trend in efficiency deterioration. Therefore, the thicknesses of  $\text{VO}_x$  of 20, 30, and 45 nm, along with an additional 5 nm  $\text{VO}_x$ , were chosen for the optimization experiment. According to the results presented in Table 1, devices using a 20 nm layer of  $\text{VO}_x$  demonstrated the best average efficiency (16.0%) compared to other devices, thus this thickness was chosen as optimal for the subsequent experiments. As was expected, devices with a 5 nm layer of  $\text{VO}_x$  demonstrated inferior characteristics, mostly due to the lower short-circuit current.

Furthermore, perovskite solar cells incorporating  $\text{WO}_x$  with 20, 40, and 60 nm thickness were fabricated. The characteristics of the devices were comparable, therefore devices with additional thicknesses of 30 and 100 nm were fabricated (100 nm is shown in Figure S3). For  $\text{WO}_x$ -based devices, no significant changes in device characteristics with the thickness increase were observed. Taking into consideration the low correlation between the material thickness and device characteristics, along with the possibility of poor perovskite surface coverage with the further decrease of the thickness, the optimal thickness of 20 nm was confirmed.

Finally, for optimization of  $\text{NbO}_x$ -based PSCs, devices using 10, 20, 30, and 40 nm thick  $\text{NbO}_x$  were studied. Devices with an  $\text{NbO}_x$  thickness lower than 30 nm were short-circuited, which was probably due to the poor coverage of perovskite and PTAA layers, resulting in direct contact with the electrode. It should also be noted that the characteristics of PSCs incorporating 30 and 40 nm of  $\text{NbO}_x$  showed poor reproducibility. The large standard deviation calculated for the characteristics of these devices may be attributed to the extremely high boiling point of  $\text{NbO}_x$ , which the PVD deposition of this material undergoes at high temperature. This in turn implies exposure of the absorber layer to elevated temperatures, which may lead to its partial thermal degradation [42]. To sum up, although PVD is not an optimal method for  $\text{NbO}_x$  deposition, a thickness of 30 nm leading to moderate efficiencies of the PSCs was confirmed as optimal for this material.

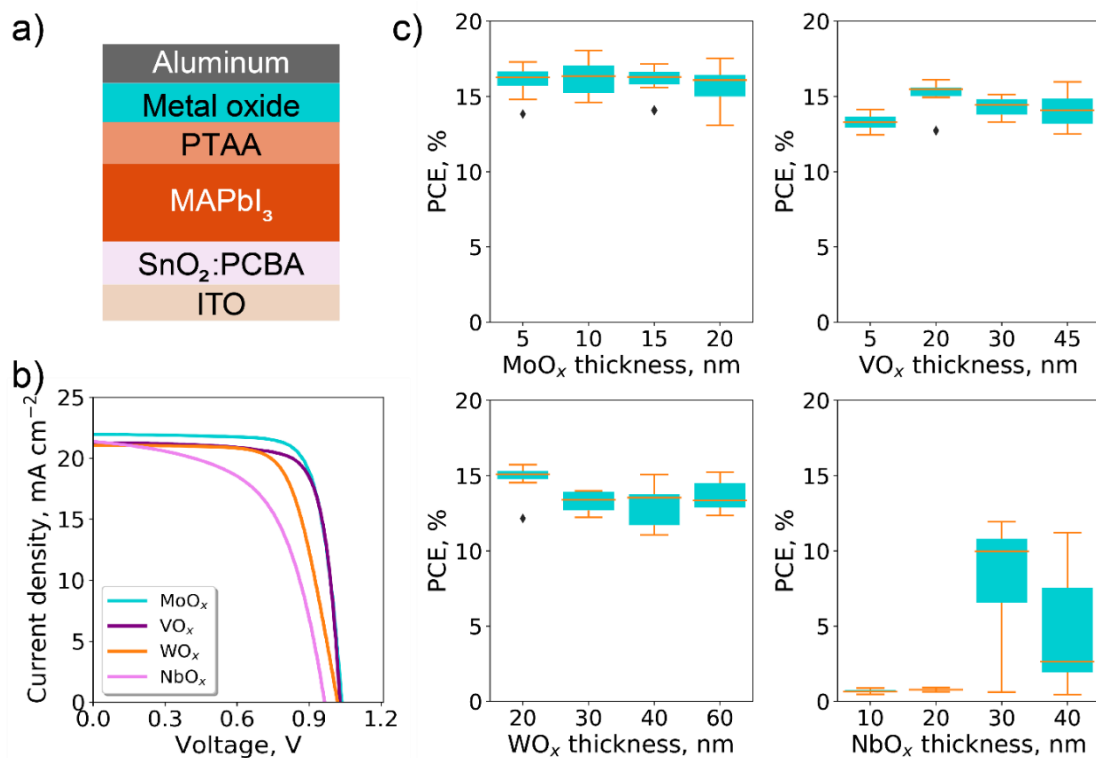


**Figure 2.** (a) Device configuration used for thickness optimization experiments; (b) current-voltage characteristics of the top cells with four metal oxides; (c) distribution of characteristics for devices with various metal oxides of various thicknesses.

Furthermore, perovskite solar cells incorporating double-layer HTLs with PTAA and  $\text{MO}_x$  with optimized thickness were investigated for stability under continuous light soaking. For this purpose, devices with an ITO electrode were covered with a ZnO ETL passivated with MAI and PCBA. Afterward, a perovskite layer with  $\text{CsFAPbI}_3$  composition was formed, and the double-layer HTL comprising PTAA was deposited using spin-coating, followed by four  $\text{MO}_x$  with optimized thicknesses being thermally evaporated under reduced pressure. The standard gold and silver electrodes were substituted with aluminum, as such modification allows improvement of the device stability at a cost of slightly reduced efficiency [7], giving the final configuration presented in Figure 3a. According to the literature, such configuration allows achieving high operational stabilities and competitive efficiencies for ZnO-based PSCs [43]. The stability evaluation was performed in the light-soaking chamber's (Figure 3b) built-in glovebox with an inert atmosphere and control of oxygen and water concentration  $<0.01$  ppm [16]. The unencapsulated devices were exposed to the constant illumination of high-power white light-emitting diodes ( $70 \pm 3$   $\text{mW}/\text{cm}^2$ ) and a temperature of  $45 \pm 1$   $^\circ\text{C}$  for 1250 h, which corresponded to the recommended degradation protocol ISOS-L-2I [44]. During the experiment, the current-voltage characteristics were collected several times; the summarized PCE evolution for devices incorporating metal oxides is presented in Figure 3c.

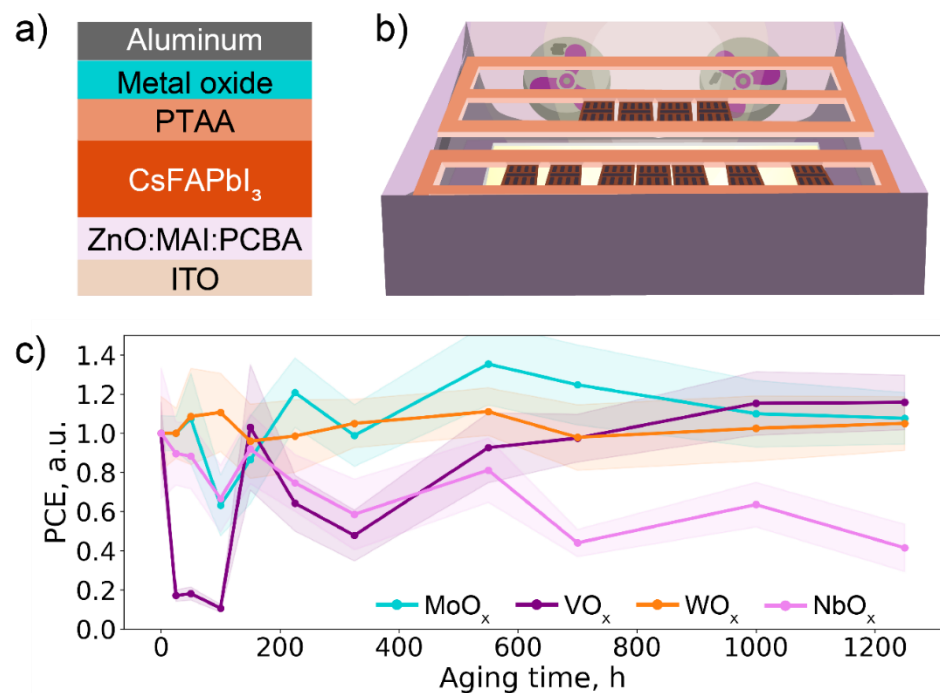


**Figure 3.** (a) Configuration of PSCs used for stability evaluation; (b) schematic layout of the light-soaking chamber; (c) comparison of PCE evolution for PSCs containing various metal oxides.

According to the results, devices using a  $\text{MoO}_x$  inorganic HTL counterpart enabled stable performance, along with slightly higher efficiencies, compared to the other materials. Similar stable performance with comparable efficiencies was observed for PSCs utilizing a  $\text{WO}_x$  interlayer. Devices including  $\text{VO}_x$  metal oxide demonstrated unusual non-monotonic behavior during the first 500 h, which could be attributed to the burn-in effect, which consists of self-healing of bulk and interfacial defects under exposure to light and temperature [45]. In addition, at 200 h, the  $\text{VO}_x$ -based PSCs reproducibly exhibited an abrupt decrease in PCE with its further restoration. The nature of this phenomenon is unknown and requires further investigation. Although the efficiencies of PSCs with  $\text{VO}_x$  are insignificantly inferior compared to devices with  $\text{MoO}_x$  and  $\text{WO}_x$ , there was a trend of a slow efficiency increase, which continued to the end of the experiment. Finally, PSCs

incorporating a  $\text{NbO}_x$  interlayer demonstrated poor stability, losing about 30% of their initial efficiency after 1000 h under illumination.

Conclusively, the three double-HTLs comprising organic polymer PTAA and thermally evaporated metals in the highest oxidizing state, namely  $\text{MoO}_x$ ,  $\text{WO}_x$ , and  $\text{VO}_x$ , demonstrated stable performance after 1250 h of continuous light soaking. The devices with  $\text{NbO}_x$  demonstrated inferior stability, which could be attributed to the high temperature of  $\text{NbO}_x$  deposition, leading to excessive substrate heating and partial thermal degradation of the perovskite layer.

To identify the encapsulating ability of PTAA/ $\text{MO}_x$  layers, the behavior of trilayer stacks with configuration glass/perovskite/PTAA/ $\text{MO}_x$  (Figure 4a) was investigated under constant illumination for 1250 h. The evolution of perovskite composition was monitored using a set of complementary techniques. In particular, the absorption spectroscopy at a 750 nm wavelength, which is characteristic for perovskite absorption, along with XRD diffractometry showing the appearance of crystalline perovskite decomposition products, were applied in this experiment [46]. The evolution of absorption at 750 nm for samples incorporating various oxides is presented in Figure 4b. For all samples, the insignificant fluctuation of absorption maximum can be observed, which can occur due to differences in the perovskite absorption along the same substrate. However, this variation was not severe enough to reach a conclusion on perovskite material decomposition. Furthermore, the XRD patterns collected after certain periods showing the evolution of material phase identification are summarized in Figure 4c. The appearance of signals at  $2\theta = 12.6^\circ$  (marked with orange stars) and  $2\theta = 31.3^\circ$  (highlighted with brown stars) was attributed to the formation of  $\text{PbI}_2$  and metallic lead phases in the photoactive layer composition, respectively. The peaks at  $2\theta = 14.2^\circ$ ,  $28.5^\circ$  and  $32.0^\circ$  were 110, 220, and 310, respectively, the most intensive peaks of the  $\text{MAPbI}_3$  cubic phase [47].

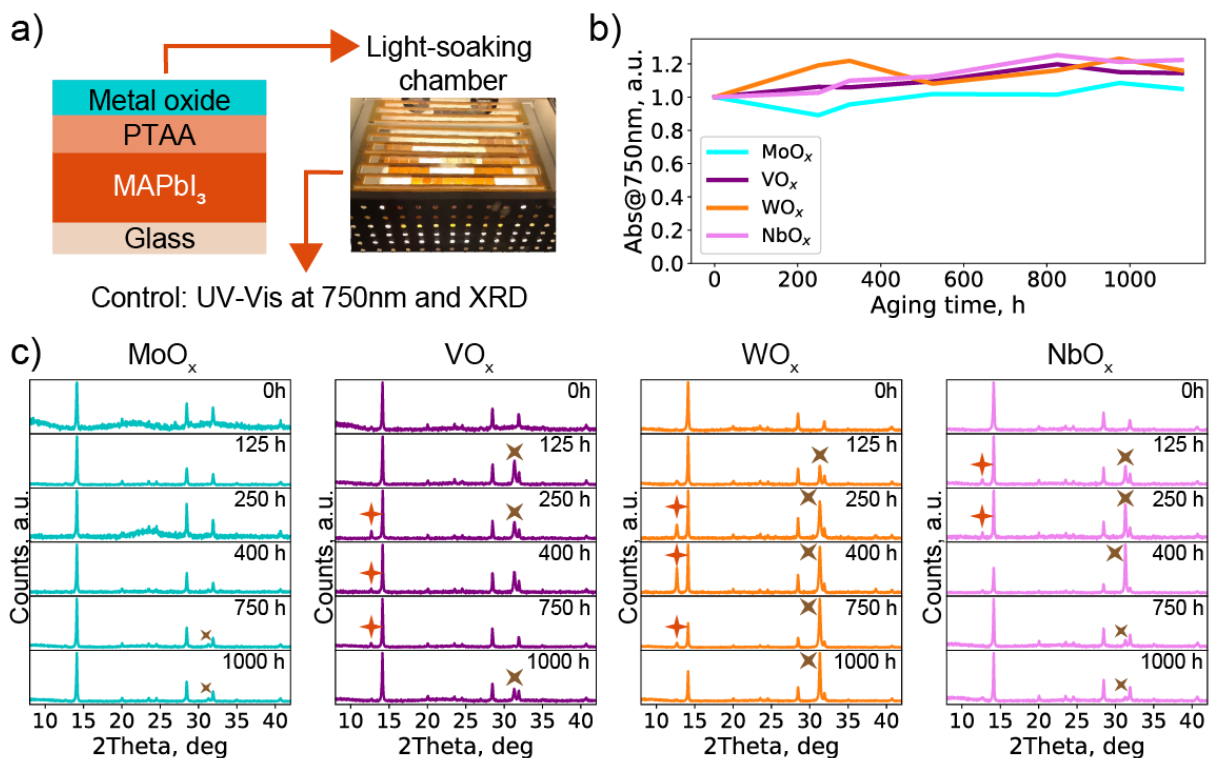


**Figure 4.** (a) Layout of the thin-film stability test experiment; (b) evolution of absorbance; (c) XRD patterns under light soaking.

According to the XRD patterns, in the sample with glass/perovskite/PTAA/MoO<sub>x</sub> composition, an insignificant amount of metallic lead was observed whereas in the stacks with VO<sub>x</sub>, WO<sub>x</sub>, and NbO<sub>x</sub>, more intensive peaks were visualized. It should be noted that in the samples with WO<sub>x</sub>, VO<sub>x</sub> and NbO<sub>x</sub>, signals of byproducts tended to both increase and decrease in intensity during the experiment, which was probably due to the proceeding of the reversible perovskite formation reaction.

In summary, all four double HTLs comprising PTAA and MO<sub>x</sub> (M = Mo, V, W, Nb) provided efficient encapsulation of the perovskite material.

In order to further investigate the encapsulating properties of PTAA/MO<sub>x</sub> organic–inorganic HTLs, time-of-flight secondary ion mass spectrometry (ToF-SIMS) experiments were conducted on the cross-sections of fresh and aged devices in the described stability experiments. ToF-SIMS is a powerful technique that allows the tracking of changes occurring in the layers of the whole device stack, thus providing insights into the relationship between the cation movement throughout the device and its effect on device stability and efficiency [48]. In this experiment, devices incorporating VO<sub>x</sub> with the configuration presented previously in Figure 3a were examined. This particular metal oxide was chosen because it exhibited the worst behavior from the stable samples, and the most severe changes in the device composition were expected. In this experiment, the sample was exposed to the focused ion beam directed at a 20° angle in order to obtain the extended cross-section. The emission of secondary ions was registered from the freshly prepared cross-section using a C-TOF detector.

Using ToF-SIMS a fresh sample and a sample after light soaking were examined, with specific consideration of particular markers assigned for each layer (Figure 5).

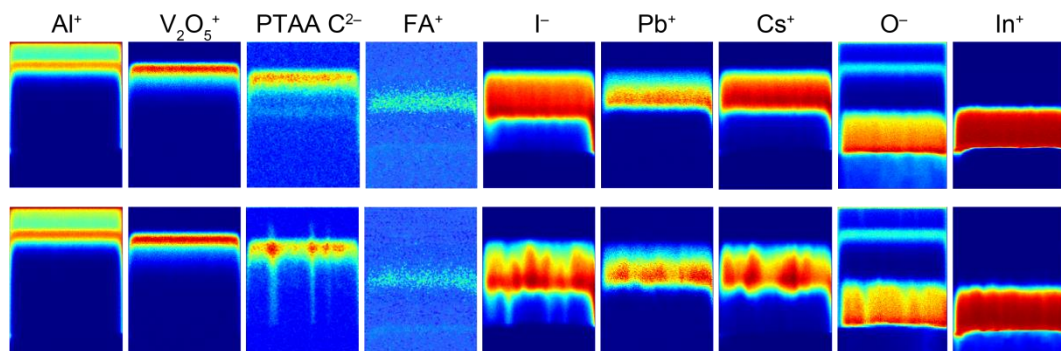


**Figure 5.** ToF-SIMS profiles showing the spatial distribution of specific markers for each layer in the PSC devices.

According to the ToF-SIMS maps, the aluminum layer with an approximately 100 nm thickness (quartz detector readings, marker Al<sup>+</sup>) and a 20 nm VO<sub>x</sub> layer (markers V<sub>2</sub>O<sub>5</sub><sup>+</sup> and O<sup>-</sup>) remain unchanged after 1250 h under illumination. The PTAA layer (about 15 nm defined using AFM) was identified with a characteristic C<sup>2-</sup> marker. Surprisingly, we observed that the organic material was not robust enough, as it partially diffused through the perovskite structure. The CsFAPbI<sub>3</sub> layer with a relative thickness lying in the interval of 300–400 nm was detected using Cs<sup>+</sup>, Pb<sup>+</sup>, I<sup>-</sup>, and CH<sub>5</sub>N<sup>+</sup> (FA) markers. The markers attributed to the volatile perovskite decomposition products such as formamidinium (CH<sub>5</sub>N<sup>+</sup>) and iodine (I<sup>-</sup>) did not breach the double HTL. The inorganic components of the perovskite material also underwent interdiffusion and mixed with lower levels and organic material. The ZnO layer (15 nm), which is not given in the figure, and commercial ITO (100–120 nm), represented here by (O<sup>-</sup> and In<sup>+</sup>), exhibited a minor transformation in the aged devices. In conclusion, according to the ToF-SIMS analysis, the double HTL prevented expansion of the perovskite and its components from the structure; however, the organic counterpart and perovskite composition should be further optimized.

#### 4. Conclusions

In this work, four double HTLs including organic polymer PTAA in combination with four transition metal oxides ( $\text{MoO}_x$ ,  $\text{VO}_x$ ,  $\text{WO}_x$ , and  $\text{NbO}_x$ ) were investigated in PSCs. The stability of PSCs incorporating four different PTAA/ $\text{MO}_x$  double HTLs was investigated for 1250 h under continuous light-soaking and temperature control. It was shown that the devices including  $\text{MoO}_x$ ,  $\text{WO}_x$ , and  $\text{VO}_x$  delivered stable performance during the experiment, and devices with  $\text{NbO}_x$  as part of HTL lost more than 30% of their initial efficiency. The non-monotonic changes of PCE during the first 200 h for devices incorporating  $\text{MoO}_x$  and  $\text{VO}_x$  require further investigation, as it may result in new methods for improving the device performance. In the next step, the ability of the double HTL to block the migration of volatile perovskite decomposition products was evaluated in trilayer stacks of perovskite covered with double HTLs. The samples were exposed to constant illumination, and changes in the absorber layer composition were monitored using UV-vis and XRD. From this experiment, the formation of small amounts of decomposition products on XRD patterns was observed, which did not lead to significant changes in the material absorbance. In addition, for most of the samples, the intensity of the byproduct peaks tended to both grow and decrease, which could indicate the reversible perovskite composition reaction. Finally, one of the devices showing stable performance for 1250 h under illumination was characterized using ToF-SIMS analysis. According to the results, the interdiffusion of perovskite decomposition products to the upper layers was not registered, which suggests good encapsulation of the perovskite layer. Additionally, the penetration of the organic layer into the photoactive layers was detected. In particular, the growth of PTAA-based filament-like structures was observed through the perovskite film, which could lead to the introduction of non-photoactive phases in the absorber material, thus affecting the device performance. Therefore, the organic component of the double HTL should be further optimized. As an appropriate alternative, one can suggest sulfur- and oxygen-containing polymers, which interact with lead in the photoactive layer by forming Lewis acid-base adducts [49], and thus maintain a robust interface with perovskite without interdiffusion. In addition, an opportunity to further improve the device performance may lie in adjustment of the perovskite composition or the synthesis of photoactive material with solvent-free approaches [50].

In summary, it was demonstrated that three metals in the highest oxidizing state deposited using physical vapor deposition, namely  $\text{MoO}_x$ ,  $\text{VO}_x$ , and  $\text{WO}_x$ , may be successfully used as inorganic counterparts of double HTL in combination with PTAA. These combinations provided high efficiencies, eliminated the requirement of p-dopants for the organic layer, and most importantly encapsulated the perovskite absorber, preventing migration of volatile decomposition products. These findings provide great impetus to bring perovskite solar cells one step forward towards the commercialization of the technology.

**Supplementary Materials:** The following are available online, Figure S1: Structures of PTAA and PCBA, Figure S2: Stability of devices with 15, 30, and 45 nm of  $\text{VO}_x$  under continuous light soaking  $70 \text{ mW}/\text{cm}^2$  and temperature  $55 \pm 3 \text{ }^\circ\text{C}$ , Figure S3: Characteristics of perovskite solar cells incorporating various thicknesses of  $\text{WO}_x$ , Figure S4: EQE for perovskite solar cells.

**Author Contributions:** Conceptualization, M.M.T., A.N.M., A.M.K. and K.J.S.; data curation, M.M.T., A.N.M., P.A.S. and E.S.S.; funding acquisition, M.M.T. and K.J.S.; investigation, M.M.T. and A.N.M.; supervision, K.J.S.; visualization, E.S.S.; writing—original draft, M.M.T.; writing—review and editing, A.M.K. and K.J.S. All authors have read and agreed to the published version of the manuscript.

**Funding:** This work was supported at Skoltech by the Russian Foundation for Basic Research (project number 19-33-90294).

**Acknowledgments:** We would like to thank Salimon A. for logistic support, and Troshin P. for sharing thoughtful ideas.

**Conflicts of Interest:** The authors declare no conflict of interest. The funders had no role in the design of the study; in the collection, analyses, or interpretation of data; in the writing of the manuscript; or in the decision to publish the results.

## References

1. Kojima, A.; Teshima, K.; Shirai, Y.; Miyasaka, T. Organometal Halide Perovskites as Visible-Light Sensitizers for Photovoltaic Cells. *J. Am. Chem. Soc.* **2009**, *131*, 6050–6051. [CrossRef]
2. NREL. Best Research-Cell Efficiency Chart. 2021. Available online: <https://www.nrel.gov/pv/cell-efficiency.html> (accessed on 15 July 2021).
3. Kim, H.-S.; Lee, C.-R.; Im, J.-H.; Lee, K.-B.; Moehl, T.; Marchioro, A.; Moon, S.-J.; Humphry-Baker, R.; Yum, J.-H.; Moser, J.E.; et al. Lead Iodide Perovskite Sensitized All-Solid-State Submicron Thin Film Mesoscopic Solar Cell with Efficiency Exceeding 9%. *Sci. Rep.* **2012**, *2*, 591. [CrossRef]
4. Lee, M.M.; Teuscher, J.; Miyasaka, T.; Murakami, T.N.; Snaith, H.J. Efficient Hybrid Solar Cells Based on Meso-Superstructured Organometal Halide Perovskites. *Science* **2012**, *338*, 643. [CrossRef]
5. Juarez-Perez, E.J.; Ono, L.K.; Maeda, M.; Jiang, Y.; Hawash, Z.; Qi, Y. Photodecomposition and thermal decomposition in methylammonium halide lead perovskites and inferred design principles to increase photovoltaic device stability. *J. Mater. Chem. A* **2018**, *6*, 9604–9612. [CrossRef]
6. Akbulatov, A.F.; Luchkin, S.Y.; Frolova, L.A.; Dremova, N.N.; Gerasimov, K.L.; Zhidkov, I.S.; Anokhin, D.V.; Kurmaev, E.Z.; Stevenson, K.J.; Troshin, P.A. Probing the Intrinsic Thermal and Photochemical Stability of Hybrid and Inorganic Lead Halide Perovskites. *J. Phys. Chem. Lett.* **2017**, *8*, 1211–1218. [CrossRef]
7. Sanehira, E.M.; Tremolet de Villers, B.J.; Schulz, P.; Reese, M.O.; Ferrere, S.; Zhu, K.; Lin, L.Y.; Berry, J.J.; Luther, J.M. Influence of Electrode Interfaces on the Stability of Perovskite Solar Cells: Reduced Degradation Using MoO<sub>x</sub>/Al for Hole Collection. *ACS Energy Lett.* **2016**, *1*, 38–45. [CrossRef]
8. Kim, G.-W.; Kang, G.; Choi, K.; Choi, H.; Park, T. Solution Processable Inorganic–Organic Double-Layered Hole Transport Layer for Highly Stable Planar Perovskite Solar Cells. *Adv. Energy Mater.* **2018**, *8*, 1801386. [CrossRef]
9. Peng, H.; Sun, W.; Li, Y.; Ye, S.; Rao, H.; Yan, W.; Zhou, H.; Bian, Z.; Huang, C. Solution processed inorganic V<sub>2</sub>O<sub>x</sub> as interfacial function materials for inverted planar-heterojunction perovskite solar cells with enhanced efficiency. *Nano Res.* **2016**, *9*, 2960–2971. [CrossRef]
10. Haider, M.; Zhen, C.; Wu, T.; Liu, G.; Cheng, H.-M. Boosting efficiency and stability of perovskite solar cells with nickel phthalocyanine as a low-cost hole transporting layer material. *J. Mater. Sci. Technol.* **2018**, *34*, 1474–1480. [CrossRef]
11. De Castro, I.A.; Datta, R.S.; Ou, J.Z.; Castellanos-Gomez, A.; Sriram, S.; Daeneke TKalantar-zadeh, K. Molybdenum Oxides—From Fundamentals to Functionality. *Adv. Mater.* **2017**, *29*, 1701619. [CrossRef]
12. Wang, J.; Zhang, J.; Meng, B.; Zhang, B.; Xie, Z.; Wang, L. Facile Preparation of Molybdenum Bronzes as an Efficient Hole Extraction Layer in Organic Photovoltaics. *ACS Appl. Mater. Interfaces* **2015**, *7*, 13590–13596. [CrossRef] [PubMed]
13. Meyer, J.; Hamwi, S.; Kröger, M.; Kowalsky, W.; Riedl TKahn, A. Transition Metal Oxides for Organic Electronics: Energetics, Device Physics and Applications. *Adv. Mater.* **2012**, *24*, 5408–5427. [CrossRef] [PubMed]
14. Gerling, L.G.; Voz, C.; Alcubilla, R.; Puigdollers, J. Origin of passivation in hole-selective transition metal oxides for crystalline silicon heterojunction solar cells. *J. Mater. Res.* **2017**, *32*, 260–268. [CrossRef]
15. You, G.; Zhuang, Q.; Wang, L.; Lin, X.; Zou, D.; Lin, Z.; Zhen, H.; Zhuang, W.; Ling, Q. Dopant-Free, Donor-Acceptor-Type Polymeric Hole-Transporting Materials for the Perovskite Solar Cells with Power Conversion Efficiencies over 20%. *Adv. Energy Mater.* **2020**, *10*, 1903146. [CrossRef]
16. Tepliakova, M.M.; Mikheeva, A.N.; Frolova, L.A.; Boldyreva, A.G.; Elakshar, A.; Novikov, A.V.; Tsarev, S.A.; Ustinova, M.I.; Yamilova, O.R.; Nasibulin, A.G.; et al. Incorporation of Vanadium(V) Oxide in Hybrid Hole Transport Layer Enables Long-term Operational Stability of Perovskite Solar Cells. *J. Phys. Chem. Lett.* **2020**, *11*, 5563–5568. [CrossRef]
17. Guo, Q.; Wang, C.; Li, J.; Bai, Y.; Wang, F.; Liu, L.; Zhang, B.; Hayat, T.; Alsaedi ATan, Z.a. Low-temperature solution-processed vanadium oxide as hole transport layer for efficient and stable perovskite solar cells. *Phys. Chem. Chem. Phys.* **2018**, *20*, 21746–21754. [CrossRef] [PubMed]
18. Schloemer, T.H.; Raiford, J.A.; Gehan, T.S.; Moot, T.; Nanayakkara, S.; Harvey, S.P.; Bramante, R.C.; Dunfield, S.; Louks, A.E.; Maughan, A.E.; et al. The Molybdenum Oxide Interface Limits the High-Temperature Operational Stability of Unencapsulated Perovskite Solar Cells. *ACS Energy Lett.* **2020**, *5*, 2349–2360. [CrossRef]
19. Yang, W.S.; Noh, J.H.; Jeon, N.J.; Kim, Y.C.; Ryu, S.; Seo JSeok, S.I. High-performance photovoltaic perovskite layers fabricated through intramolecular exchange. *Science* **2015**, *348*, 1234. [CrossRef] [PubMed]
20. Pitchaiya, S.; Natarajan, M.; Santhanam, A.; Asokan, V.; Yuvapragasam, A.; Madurai Ramakrishnan, V.; Palanisamy, S.E.; Sundaram SVelauthapillai, D. A review on the classification of organic/inorganic/carbonaceous hole transporting materials for perovskite solar cell application. *Arab. J. Chem.* **2020**, *13*, 2526–2557. [CrossRef]
21. Gao, L.; Schloemer, T.H.; Zhang, F.; Chen, X.; Xiao, C.; Zhu, K.; Sellinger, A. Carbazole-Based Hole-Transport Materials for High-Efficiency and Stable Perovskite Solar Cells. *ACS Appl. Energy Mater.* **2020**, *3*, 4492–4498. [CrossRef]
22. Yao, X.; Xu, W.; Huang, X.; Qi, J.; Yin, Q.; Jiang, X.; Huang, F.; Gong, X.; Cao, Y. Solution-processed vanadium oxide thin film as the hole extraction layer for efficient hysteresis-free perovskite hybrid solar cells. *Org. Electron.* **2017**, *47*, 85–93. [CrossRef]

23. Tseng, Z.L.; Chen, L.C.; Chiang, C.H.; Chang, S.H.; Chen, C.C.; Wu, C.G. Efficient inverted-type perovskite solar cells using UV-ozone treated MoO<sub>x</sub> and WO<sub>x</sub> as hole transporting layers. *Sol. Energy* **2016**, *139*, 484–488. [[CrossRef](#)]
24. Chen, L.; Xie, Q.; Wan, L.; Zhang, W.; Fu, S.; Zhang, H.; Ling, X.; Yuan, J.; Miao, L.; Shen, C.; et al. Solution-Processed MoO<sub>x</sub> Hole-Transport Layer with F4-TCNQ Modification for Efficient and Stable Inverted Perovskite Solar Cells. *ACS Appl. Energy Mater.* **2019**, *2*, 5862–5870. [[CrossRef](#)]
25. Hou, F.; Su, Z.; Jin, F.; Yan, X.; Wang, L.; Zhao, H.; Zhu, J.; Chu, B.; Li, W. Efficient and stable planar heterojunction perovskite solar cells with an MoO<sub>3</sub>/PEDOT:PSS hole transporting layer. *Nanoscale* **2015**, *7*, 9427. [[CrossRef](#)]
26. Zhang, L.; Liu, C.; Zhang, J.; Li, X.; Cheng, C.; Tian, Y.; Jen, A.K.; Xu, B. Intensive Exposure of Functional Rings of a Polymeric Hole-Transporting Material Enables Efficient Perovskite Solar Cells. *Adv. Mater.* **2018**, *30*, 1–7. [[CrossRef](#)]
27. Liu, Z.; He, T.; Wang, H.; Song, X.; Liu, H.; Yang, J.; Liu, K.; Ma, H. Improving the stability of the perovskite solar cells by V<sub>2</sub>O<sub>5</sub> modified transport layer film. *RSC Adv.* **2017**, *7*, 18456–18465. [[CrossRef](#)]
28. Duan, C.; Zhao, M.; Zhao, C.; Wang, Y.; Li, J.; Han, W.; Hu, Q.; Yao, L.; Jian, H.; Lu, F.; et al. Inverted CH<sub>3</sub>NH<sub>3</sub>PbI<sub>3</sub> perovskite solar cells based on solution-processed V<sub>2</sub>O<sub>5</sub> film combined with P3CT salt as hole transport layer. *Mater. Today Energy* **2018**, *9*, 487–495. [[CrossRef](#)]
29. Raiford, J.A.; Belisle, R.A.; Bush, K.A.; Prasanna, R.; Palmstrom, A.F.; McGehee, M.D.; Bent, S.F. Atomic layer deposition of vanadium oxide to reduce parasitic absorption and improve stability in n–i–p perovskite solar cells for tandems. *Sustain. Energy Fuels* **2019**, *3*, 1517–1525. [[CrossRef](#)]
30. Kim, J.; Kim, G.; Back, H.; Kong, J.; Hwang, I.-W.; Kim, T.K.; Kwon, S.; Lee, J.-H.; Lee, J.; Yu, K.; et al. High-Performance Integrated Perovskite and Organic Solar Cells with Enhanced Fill Factors and Near-Infrared Harvesting. *Adv. Mater.* **2016**, *28*, 3159–3165. [[CrossRef](#)]
31. Chang, C.-C.; Tao, J.-H.; Tsai, C.-E.; Cheng, Y.-J.; Hsu, C.-S. Cross-linked Triarylamine-Based Hole-Transporting Layer for Solution-Processed PEDOT:PSS-Free Inverted Perovskite Solar Cells. *ACS Appl. Mater. Interfaces* **2018**, *10*, 21466–21471. [[CrossRef](#)]
32. Eze, V.O.; Seike, Y.; Mori, T. Efficient planar perovskite solar cells using solution-processed amorphous WO<sub>x</sub>/fullerene C<sub>60</sub> as electron extraction layers. *Org. Electron.* **2017**, *46*, 253–262. [[CrossRef](#)]
33. Liu, P.; Wang, C.; Zhou, D.; Yuan, Q.; Wang, Y.; Hu, Y.; Han, D.; Feng, L. Wox@Pedot Core–Shell Nanorods: Hybrid Hole-Transporting Materials for Efficient and Stable Perovskite Solar Cells. *ACS Appl. Energy Mater.* **2018**, *1*, 1742–1752. [[CrossRef](#)]
34. Yi, H.; Wang, D.; Duan, L.; Haque, F.; Xu, C.; Zhang, Y.; Conibeer, G.; Uddin, A. Solution-processed WO<sub>3</sub> and water-free PEDOT:PSS composite for hole transport layer in conventional perovskite solar cell. *Electrochim. Acta* **2019**, *319*, 349–358. [[CrossRef](#)]
35. Vasilopoulou, M.; Palilis, L.C.; Georgiadou, D.G.; Douvas, A.M.; Argitis, P.; Kennou, S.; Sygellou, L.; Papadimitropoulos, G.; Kostis, I.; Stathopoulos, N.A.; et al. Reduction of Tungsten Oxide: A Path towards Dual Functionality Utilization for Efficient Anode and Cathode Interfacial Layers in Organic Light-Emitting Diodes. *Adv. Funct. Mater.* **2011**, *21*, 1489–1497. [[CrossRef](#)]
36. Tepliakova, M.; Yakushenko, I.K.; Romadina, E.I.; Novikov, A.V.; Kuznetsov, P.M.; Stevenson, K.J.; Troshin, P.A. Strength of attraction: Pyrene-based hole-transport materials with effective  $\pi$ – $\pi$  stacking for dopant-free perovskite solar cells. *Sustain. Energy Fuels* **2021**, *5*, 283–288. [[CrossRef](#)]
37. Ouyang, Y.; Li, Y.; Zhu, P.; Li, Q.; Gao, Y.; Tong, J.; Shi, L.; Zhou, Q.; Ling, C.; Chen, Q.; et al. Photo-oxidative degradation of methylammonium lead iodide perovskite: Mechanism and protection. *J. Mater. Chem. A* **2019**, *7*, 2275–2282. [[CrossRef](#)]
38. Ouyang, Y.; Shi, L.; Li, Q.; Wang, J. Role of Water and Defects in Photo-Oxidative Degradation of Methylammonium Lead Iodide Perovskite. *Small Methods* **2019**, *3*, 1900154. [[CrossRef](#)]
39. Hummelen, J.C.; Knight, B.W.; LePeq, F.; Wudl, F.; Yao, J.; Wilkins, C.L. Preparation and Characterization of Fulleroid and Methanofullerene Derivatives. *J. Org. Chem.* **1995**, *60*, 532–538. [[CrossRef](#)]
40. Tepliakova, M.M.; Akkuratov, A.V.; Tsarev, S.A.; Troshin, P.A. Suzuki polycondensation for the synthesis of polytriarylamines: A method to improve hole-transport material performance in perovskite solar cells. *Tetrahedron Lett.* **2020**, *61*, 152317. [[CrossRef](#)]
41. Tsarev, S.; Dubinina, T.S.; Luchkin, S.Y.; Zhidkov, I.S.; Kurmaev, E.Z.; Stevenson, K.J.; Troshin, P.A. Phenyl-C61-butyric Acid as an Interface Passivation Layer for Highly Efficient and Stable Perovskite Solar Cells. *J. Phys. Chem. C* **2020**, *124*, 1872–1877. [[CrossRef](#)]
42. Emeka, N.C.; Imoisili, P.E.; Jen, T.-C. Preparation and Characterization of Nb<sub>x</sub>O<sub>y</sub> Thin Films: A Review. *Coatings* **2020**, *10*, 1246. [[CrossRef](#)]
43. Tsarev, S.; Olthof, S.; Boldyreva, A.G.; Aldoshin, S.M.; Stevenson, K.J.; Troshin, P.A. Reactive modification of zinc oxide with methylammonium iodide boosts the operational stability of perovskite solar cells. *Nano Energy* **2021**, *83*, 105774. [[CrossRef](#)]
44. Khenkin, M.V.; Katz, E.A.; Abate, A.; Bardizza, G.; Berry, J.J.; Brabec, C.; Brunetti, F.; Bulović, V.; Burlingame, Q.; Di Carlo, A.; et al. Consensus statement for stability assessment and reporting for perovskite photovoltaics based on ISOS procedures. *Nat. Energy* **2020**, *5*, 35–49. [[CrossRef](#)]
45. Christians, J.A.; Schulz, P.; Tinkham, J.S.; Schloemer, T.H.; Harvey, S.P.; Tremolet de Villers, B.J.; Sellinger, A.; Berry, J.J.; Luther, J.M. Tailored interfaces of unencapsulated perovskite solar cells for >1000 hour operational stability. *Nat. Energy* **2018**, *3*, 68–74. [[CrossRef](#)]
46. Boldyreva, A.G.; Akbulatov, A.F.; Elnaggar, M.; Luchkin, S.Y.; Danilov, A.V.; Zhidkov, I.S.; Yamilova, O.R.; Fedotov, Y.S.; Bredikhin, S.I.; Kurmaev, E.Z.; et al. Impact of charge transport layers on the photochemical stability of MAPbI<sub>3</sub> in thin films and perovskite solar cells. *Sustain. Energy Fuels* **2019**, *3*, 2705–2716. [[CrossRef](#)]

47. Oku, T. *Crystal Structures of CH<sub>3</sub>NH<sub>3</sub>PbI<sub>3</sub> and Related Perovskite Compounds Used for Solar Cells, Solar Cells—New Approaches and Reviews*; IntechOpen: London, UK, 2015.
48. Harvey, S.P.; Li, Z.; Christians, J.A.; Zhu, K.; Luther, J.M.; Berry, J.J. Probing Perovskite Inhomogeneity beyond the Surface: TOF-SIMS Analysis of Halide Perovskite Photovoltaic Devices. *ACS Appl. Mater. Interfaces* **2018**, *10*, 28541–28552. [[CrossRef](#)] [[PubMed](#)]
49. Wang, S.; Wang, A.; Deng, X.; Xie, L.; Xiao, A.; Li, C.; Xiang, Y.; Li, T.; Ding, L.; Hao, F. Lewis acid/base approach for efficacious defect passivation in perovskite solar cells. *J. Mater. Chem. A* **2020**, *8*, 12201–12225. [[CrossRef](#)]
50. López, C.A.; Abia, C.; Rodrigues, J.E.; Serrano-Sánchez, F.; Nemes, N.M.; Martínez, J.L.; Fernandez-Díaz, M.T.; Biškup, N.; Alvarez-Galván, C.; Carrascoso, F.; et al. Enhanced Stability in CH<sub>3</sub>NH<sub>3</sub>PbI<sub>3</sub> Hybrid Perovskite from Mechano-Chemical Synthesis: Structural, Microstructural and Optoelectronic Characterization. *Sci. Rep.* **2020**, *10*, 11228. [[CrossRef](#)]